Stability Analysis of Converter Control Modes in Low-Inertia Power Systems

Uros Markovic*, Johanna Vorwerk*, Petros Aristidou§, Gabriela Hug*
* EEH - Power Systems Laboratory, ETH Zurich, Physikstrasse 3, 8092 Zurich, Switzerland
§ School of Electronic and Electrical Engineering, University of Leeds, Leeds LS2 9JT, UK
Emails: {markovic, hug}@eeh.ee.ethz.ch, vorwerkj@student.ethz.ch, p.aristidou@leeds.ac.uk

***Abstract*—This paper deals with the small-signal stability analysis of converter control modes in low-inertia power systems. For this purpose, a detailed differential-algebraic equation model of the voltage source converter and its control scheme is developed. Both grid-forming and grid-feeding concepts have been considered, as well as different active power controllers based on traditional droop and virtual inertia emulation. An eigenvalue analysis of the linearized state-space system is conducted and the performance of different control configurations is compared. Furthermore, various bifurcation studies have been completed and conclusions on stability margins have been drawn with respect to control sensitivity and robustness.**

***Index Terms*—voltage source converter (VSC), virtual inertia emulation, small-signal stability, low-inertia systems**

I. Introduction

The penetration of Voltage Source Converters (VSCs) in power systems is drastically increasing, with them acting as a grid interface for emerging renewable generation. As they are based on power electronics, the physical inertia of the generators is now electrically decoupled from the network, resulting in low-inertia systems and imposing new challenges regarding system stability [1]. In order to capture the system dynamics in the presence of converters, new Differential-Algebraic Equation (DAE) models must be developed for the purposes of small-signal analysis.

The work in [2] investigated the stability of a VSC control scheme based on the virtual swing equation. However, there was no external power control included in the model, and the implementation of the damping restricted the applicability of the studied control system. An extension of this control design was presented in [3], where a frequency droop was included in the outer loop, together with the Phase Locked Loop (PLL) and virtual impedance. The same control system and the corresponding small-signal model was further elaborated and analyzed in [4]. Nonetheless, both approaches focus on a single power control design and put emphasis on the grid-connected operation only. Since the potential VSC control configurations [5]–[7], as well as the operation modes [8], [9] can be quite versatile, requirements for a more general modeling approach are emerging.

The contribution of this work is two-fold. First, we introduce a uniform VSC model with a detailed, state-of-the-art control structure. Two active power control approaches are proposed under different converter operation modes. Subsequently, an analytical formulation of the DAE system, together with the respective small-signal model is derived. Second, the stability margins of different VSC configurations are investigated through eigenvalue analysis and various bifurcation studies.

The remainder of the paper is structured as follows. In Section II, a detailed VSC control scheme is presented, as well as the respective analytical formulation of the DAEs. Section III describes the small-signal modeling and state-space representation. Section IV showcases the stability analyses results, whereas Section V concludes the paper.

II. VSC Control Scheme

An overview of the implemented converter control scheme is shown in Fig. 1, where a VSC is connected to a constant active power load and a grid through a Low-Pass Filter (LPF) and a transformer. The outer control loop consists of active and reactive power controllers, which provide the output voltage angle and magnitude reference by adjusting the predefined setpoints according to a measured power imbalance. The reference voltage vector signal is sent to the inner control loop consisting of cascaded voltage and current controllers operating in a Synchronously-rotating Reference Frame (SRF). In order to detect the system frequency at the Point of Common Coupling (PCC), a PLL-based synchronization unit is included in the model.

The complete modeling, analysis and control of the converter is implemented in an SRF, with the (abc/dq)-block denoting a sequence of power-invariant Clarke ($\boldsymbol{T}_c$) and Park ($\boldsymbol{T}_p$) transformations from a stationary (abc)-frame to the SRF:

$$\boldsymbol{x}^{dq} = \underbrace{\sqrt{\frac{2}{3}}\begin{bmatrix}\cos\theta & \cos\left(\theta-\frac{2\pi}{3}\right) & \cos\left(\theta+\frac{2\pi}{3}\right)\\ \sin\theta & \sin\left(\theta-\frac{2\pi}{3}\right) & \sin\left(\theta+\frac{2\pi}{3}\right)\end{bmatrix}}_{\boldsymbol{T}_p\boldsymbol{T}_c}\boldsymbol{x}^{abc} \quad (1)$$

It should be noted that the mathematical model is defined in per unit (denoted by lower-case symbols), and the quantities in the (dq)-frame are described in complex space vector form:

$$\boldsymbol{x} \equiv \boldsymbol{x}^{dq} = x^d + jx^q \quad (2)$$

with the dq superscript omitted in the remainder of the paper. Furthermore, the external control setpoints, e.g., the active power reference, are marked with x^*, whereas the internally

This project has received funding from the *European Union's Horizon 2020 research and innovation programme* under grant agreement No 691800. This paper reflects only the authors' views and the European Commission is not responsible for any use that may be made of the information it contains.

978-1-5386-4505-5/18/$31.00

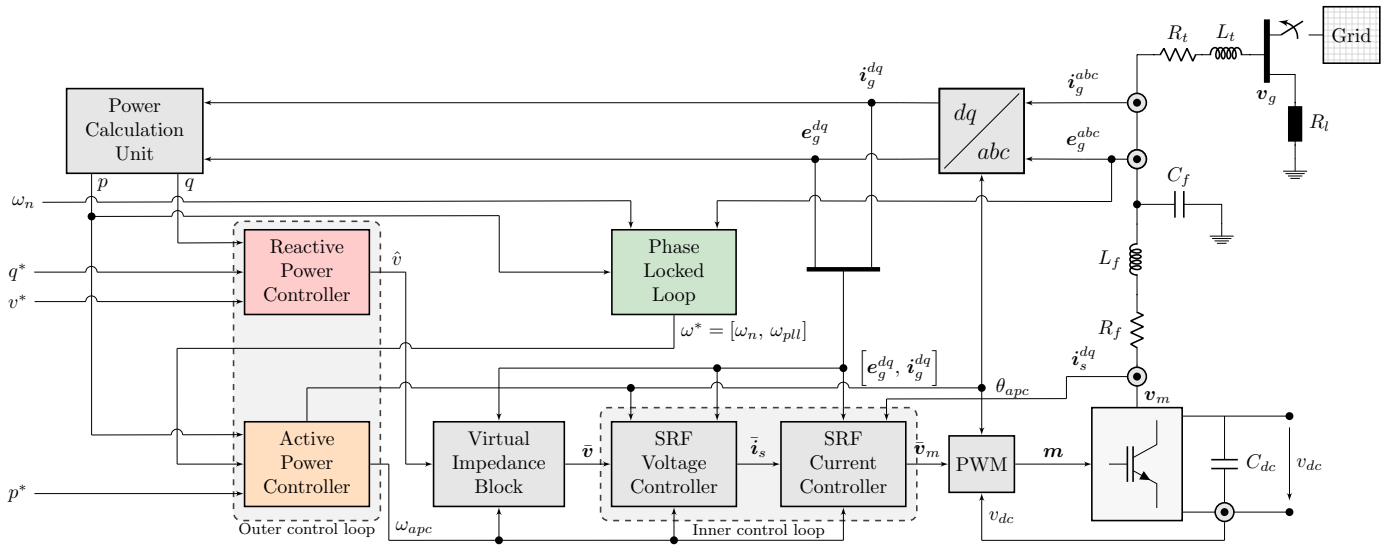

Fig. 1: Investigated system configuration and VSC control structure.

computed references are represented as $\bar{x}$. The configuration of the aforementioned main control blocks is depicted in Fig. 2, while the mathematical formulation of the proposed DAE model is elaborated in more detail below.

A. Electrical System and Power Calculation

The VSC can be operated in islanded and grid-connected mode through a switch operation, as indicated in Fig.1. In both cases, the electrical system includes an LPF (r_f, l_f, c_f) and a transformer equivalent (r_t, l_t) to model the respective copper and iron losses. Hence, the SRF state-space equations for the grid-connected case are formulated as follows:

$$\dot{\boldsymbol{i}}_s = \frac{\omega_b}{l_f}(\boldsymbol{v}_m - \boldsymbol{e}_g) - \left(\frac{r_f}{l_f}\omega_b + j\omega_b\omega_g\right)\boldsymbol{i}_s \tag{3}$$

$$\dot{\boldsymbol{i}}_g = \frac{\omega_b}{l_g + l_t}(\boldsymbol{e}_g - \boldsymbol{v}_g) - \left(\frac{r_g + r_t}{l_g + l_t}\omega_b + j\omega_b\omega_g\right)\boldsymbol{i}_g \tag{4}$$

$$\dot{\boldsymbol{e}}_g = \frac{\omega_b}{c_f}(\boldsymbol{i}_s - \boldsymbol{i}_g) - j\omega_g\omega_b\boldsymbol{e}_g \tag{5}$$

where $\boldsymbol{i}_s$ is the switching current flowing through the filter inductance, $\boldsymbol{v}_m$ is the modulation voltage at the converter output, $\boldsymbol{i}_g$ is the current flowing into the grid, $\boldsymbol{e}_g$ is the output voltage across the filter capacitance, and $\boldsymbol{v}_g$ is the voltage of the grid equivalent. The resistance and inductance of the grid are denoted as r_g and l_g, while the grid and base frequency are represented as ω_g and ω_b, respectively. For the sake of simplicity, the electric system is modeled in the SRF defined by the Active Power Control (APC).

The analysis of an islanded operation mode can be done by replacing the expression (4) with:

$$\dot{\boldsymbol{i}}_g = \frac{\omega_b}{l_t}(\boldsymbol{e}_g - \boldsymbol{v}_g) - \left(\frac{r_t}{l_t}\omega_b + j\omega_b\omega_g\right)\boldsymbol{i}_g \tag{6}$$

$$\boldsymbol{v}_g = r_l\boldsymbol{i}_g = \frac{v_l^2}{p_l}\boldsymbol{i}_g \tag{7}$$

while defining the active load as a function of active power consumption (p_l) and constant voltage amplitude (v_l). Finally, the power calculation block computes the active and reactive power output of the converter by processing the measurements of voltage and current after the filter:

$$p = \Re(\boldsymbol{e}_g\boldsymbol{i}_g^*) \quad , \quad q = \Im(\boldsymbol{e}_g\boldsymbol{i}_g^*) \tag{8}$$

with $\boldsymbol{i}_g^*$ being a complex conjugate of the grid current.

B. Phase-Locked Loop

The synchronization unit is implemented as a Type-2 PLL, which estimates the grid frequency and keeps the VSC synchronized in a grid-feeding mode of operation [10]. A PLL acts as an observer and tracks the frequency by measuring the stationary output voltage $(\boldsymbol{e}_g^{abc})$, transforming it into an internal (dq)-frame $(\hat{\boldsymbol{e}}_g)$, and passing it through a PI-controller that acts on the phase angle difference. The synchronization is achieved by aligning the d-axis of the internal SRF with the stationary (abc)-frame and diminishing the q-component, as described in [9]. A mathematical formulation is presented in (9)-(11), and a detailed control structure is given in Fig. 2a.

$$\omega_{pll} = \omega_n + K_p^{pll}\hat{e}_g^q + K_i^{pll}\varepsilon \tag{9}$$

$$\dot{\varepsilon} = \hat{e}_g^q \tag{10}$$

$$\dot{\theta}_{pll} = \omega_{pll}\omega_b \tag{11}$$

The estimated frequency and angle are represented as ω_{pll} and θ_{pll}, whereas ω_n and ε are the nominal frequency and integrator state, respectively. It should be noted that the Park transformation within the PLL is completely independent of the transformation used for the electrical circuit in Section II-A, and therefore introduces a second SRF into the system. Hence, the internally computed output voltage is denoted as $\hat{\boldsymbol{e}}_g$.

C. Active Power Control

Since the focus of this work is on converter operation on a transmission grid level, the active power control has

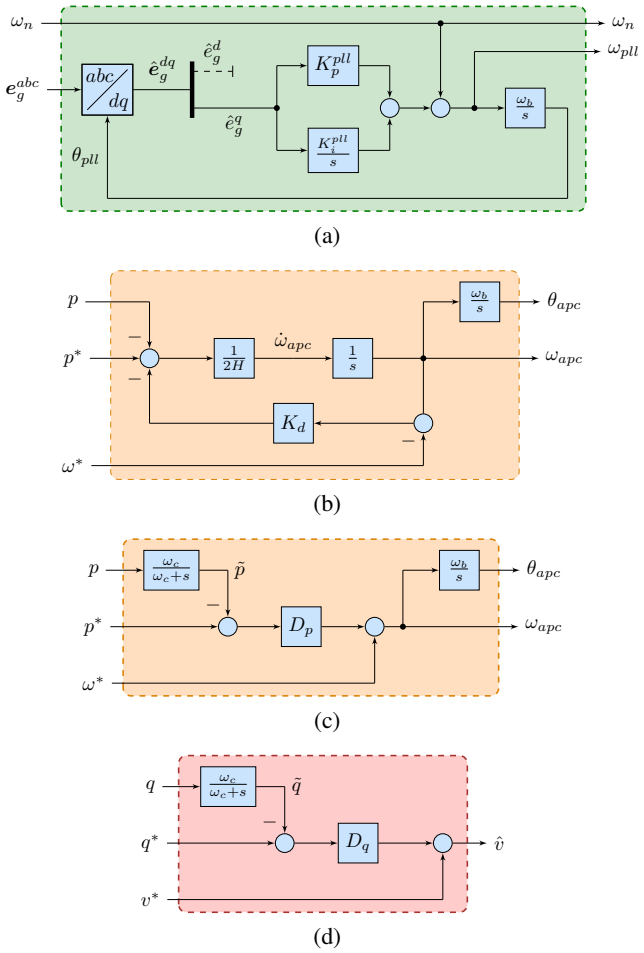

Fig. 2: Main control blocks of the converter control scheme: (a) phase-locked loop; (b) active power controller emulating virtual inertia; (c) droop-based active power controller; (d) reactive power controller.

been realized using two different approaches: (i) traditional droop control based on the strong coupling of active power and frequency; (ii) Virtual Inertia Emulation (VIE) through replicating the swing equation [11], [12]. The two control architectures can be proven mathematically equivalent under certain steady-state conditions [3], whereas VIE offers overall better behavior during frequency transients [8].

For Active Power Droop Control (APDC), the measured active power signal is passed through a first-order LPF with a cut-off frequency ω_c. Subsequently, the active power droop gain (D_p) regulates the output frequency (ω_{apc}) based on the mismatch between the filtered power measurement signal $(\tilde{p})$ and the external setpoint (p^*), as follows:

$$\omega_{apc} = \omega^* + D_p(p^* - \tilde{p}) \tag{12}$$

$$\dot{\tilde{p}} = \omega_c(p - \tilde{p}) \tag{13}$$

On the other hand, the VIE is based on a linearized form of the conventional swing equation, representing the relation between physical inertia and damping of a synchronous machine. Hence, the frequency can be expressed via a differential equation of the form:

$$\dot{\omega}_{apc} = \frac{1}{2H}\underbrace{(p^* - p)}_{p_m - p_e} - \frac{1}{2H}\underbrace{K_d(\omega_{apc} - \omega^*)}_{p_d} \tag{14}$$

where the mechanical (p_m) and electrical (p_e) power of a synchronous machine are replaced by the active power setpoint (p^*) and power output fed into the grid (p), respectively. The damping term is incorporated through a feedback loop, with a damping constant (K_d) being the feedback gain imposed on the frequency mismatch, while a normalized inertia constant (H) determines the rate-of-change-of frequency during transients. The block diagram implementation of the two control approaches is presented in Fig. 2b-2c, with the corresponding steady-state equivalence between the two APC parameters as follows [3]:

$$H = \frac{1}{2\omega_c D_p} \quad , \quad K_d = \frac{1}{D_p} \tag{15}$$

Furthermore, the corresponding phase angle (θ_{apc}) of the APC-based SRF is used as a reference angle for the (dq)-transformation of the entire system, with exclusion of the PLL, i.e.

$$\dot{\theta}_{apc} = \omega_{apc}\omega_b \tag{16}$$

In case the converter is operating in an islanded mode, the APC establishes the "grid" frequency, thus omitting the need for a synchronization unit and simplifying the problem. In other words, the grid-forming $(g$-form) VSC is modeled with the PLL block simply passing through the nominal frequency signal as a new APC setpoint $(\omega^* = \omega_n)$, whereas in the grid-feeding $(g$-feed) case the frequency setpoint is being actively observed $(\omega^* = \omega_{pll})$.

D. Reactive Power Control

Analogous to the APC, the strong coupling of reactive power and voltage enables a droop-based implementation of reactive power control. The desired output voltage $(\hat{v})$ is computed as an adjustment of the voltage setpoint (v^*), according to a mismatch in the reactive power:

$$\hat{v} = v^* + D_q(q^* - \tilde{q}) \tag{17}$$

$$\dot{\tilde{q}} = \omega_c(q - \tilde{q}) \tag{18}$$

with q, $\tilde{q}$ and q^* denoting the actual, LPF and setpoint value of the reactive power, respectively, and D_q being the reactive power droop gain. The control block configuration is given in Fig. 2d.

E. Virtual Impedance

The virtual impedance concept is increasingly used for the control of power electronic systems, either embedded as an additional degree of freedom for active stabilization and disturbance rejection, or employed as a command reference generator for the converters to provide ancillary services [13]. This paper incorporates the virtual impedance in order to split the voltage reference into (dq)-components, before passing

it to the inner control loop. Despite maximizing the active power output when set to zero, a non-zero q-component is necessary to allow for "acceleration" and "deceleration" of the virtual machine. Therefore, a minor cross-coupling of d- and q-components is included via the resistive (r_v) and inductive (l_v) elements. While the former is set to $r_v = 0$ for simplicity, the latter should be kept as small as possible, yielding the respective d-axis and q-axis voltage components:

$$\bar{v}^d = \hat{v} - r_v i_g^d + \omega_{apc} l_v i_g^q \tag{19}$$

$$\bar{v}^q = -r_v i_g^q + \omega_{apc} l_v i_g^d \tag{20}$$

which are directly used as reference inputs for the decoupling SRF voltage controller.

F. Inner Control Loop and Modulation

The computed references for voltage, frequency and alignment angle are passed to the inner control loop, as indicated in Fig.1. However, a direct use of such signals for Pulse-Width Modulation (PWM) raises problems regarding the limitations and controlled saturation of the converter's currents and voltages [14]. These issues are conveniently resolved with a cascaded inner control scheme where the initial reference $(\bar{\boldsymbol{v}})$ is processed through a sequence of voltage and current loops, yielding a more robust converter setpoint $(\bar{\boldsymbol{v}}_m)$. Such approach increases the flexibility of protection strategies and is commonly used in droop-controlled microgrids [7], [15].

1) SRF Voltage Control: The structure of the SRF voltage controller follows the similar principles as the controllers in [3], [14]:

$$\bar{\boldsymbol{i}}_s = K_p^v(\bar{\boldsymbol{v}} - \boldsymbol{e}_g) + K_i^v \boldsymbol{\xi} + j\omega_{apc} c_f \boldsymbol{e}_g + K_f^i \boldsymbol{i}_g \tag{21}$$

$$\dot{\boldsymbol{\xi}} = \bar{\boldsymbol{v}} - \boldsymbol{e}_g \tag{22}$$

where K_p^v and K_i^v are the proportional and integral gains of the SRF voltage PI controller, and $\boldsymbol{\xi}$ is the integrator state. Furthermore, a feed-forward signal of the measured currents can be enabled or disabled by changing the gain $K_f^i \in [0,\, 1]$. The output current reference $(\bar{\boldsymbol{i}}_s)$ is then used as an input setpoint to the current controller.

2) SRF Current Control: Similar to its voltage counterpart, the configuration of the SRF current controller is based on a PI control with decoupling terms:

$$\bar{\boldsymbol{v}}_m = K_p^i(\bar{\boldsymbol{i}}_s - \boldsymbol{i}_s) + K_i^i \boldsymbol{\gamma} + j\omega_{apc} l_f \boldsymbol{i}_s + K_f^v \boldsymbol{e}_g \tag{23}$$

$$\dot{\boldsymbol{\gamma}} = \bar{\boldsymbol{i}}_s - \boldsymbol{i}_s \tag{24}$$

with K_p^i, K_i^i and K_f^v being the respective controller gains, and $\boldsymbol{\gamma}$ the integrator state. The generated output voltage reference $(\bar{\boldsymbol{v}}_m)$ is used to determine the final modulation signal as explained in the following subsection.

3) Pulse-Width Modulation: For the purpose of an actual implementation of the VSC switching sequence, the voltage reference signal $(\bar{\boldsymbol{v}}_m)$ from the current controller must be processed and converted into the modulation index $(\boldsymbol{m})$. This can be achieved through means of instantaneous averaging applied to the output voltage of the converter. Furthermore, the time delay effect of PWM is neglected, which yields the following expression:

$$\boldsymbol{m}^{abc} = (\boldsymbol{T}_p \boldsymbol{T}_c)^{-1} \boldsymbol{m}^{dq} = (\boldsymbol{T}_p \boldsymbol{T}_c)^{-1} \frac{\bar{\boldsymbol{v}}_m}{v_{dc}} \tag{25}$$

The inclusion of the DC voltage (v_{dc}) enables the averaging and ensures that the actual VSC output is close to the initial reference. Additionally, it reduces the AC side sensitivity to the oscillations of the DC voltage [3].

G. Synchronization and SRF Alignment

Since the entire control system is implemented in the SRF defined by the APC, all states in the presented model rotate with frequency ω_{apc}. However, the same does not apply to the states included in the PLL unit, as described in Section II-B. Therefore, the two transformations have to be properly aligned.

This can be achieved by expressing the two SRFs respective of the common reference vector, i.e., the measured output voltage $(\boldsymbol{e}_g)$, as presented in Fig. 3. By introducing the angular speed $(\nu_{apc},\, \nu_{pll})$ and phase angle $(\vartheta_{apc},\, \vartheta_{pll})$ displacement of the respective rotating frames, we can reformulate the expressions in (9), (11) and (16) as:

$$\nu_{pll} = \omega_n - \omega_g + K_p^{pll} \hat{e}_g^q + K_i^{pll} \varepsilon \tag{26}$$

$$\dot{\vartheta}_{pll} = \nu_{pll} \omega_b \tag{27}$$

$$\dot{\vartheta}_{apc} = \nu_{apc} \omega_b \tag{28}$$

where, assuming the notation $x_k \in \{x_{pll}, x_{apc}\}$, we define

$$\nu_k = \omega_k - \omega_g \quad , \quad \vartheta_k = \theta_k - \theta_g \tag{29}$$

Here, ω_g and θ_g refer to the angular speed and position of the grid voltage vector. Furthermore, the phase angle difference between the two SRFs is equal to $\Delta\vartheta = \vartheta_{apc} - \vartheta_{pll}$, which provides the transformation of the internal PLL vector $\hat{\boldsymbol{e}}_g$ into an APC-based SRF:

$$\hat{\boldsymbol{e}}_g = \boldsymbol{e}_g e^{-(\vartheta_{pll} - \vartheta_{apc})} \tag{30}$$

Finally, the reformulation of $\hat{e}_g^q$ term in (10) concludes the alignment, as all states are transformed into a uniform SRF.

$$\dot{\varepsilon} = e_g^d \sin(\vartheta_{apc} - \vartheta_{pll}) + e_g^q \cos(\vartheta_{pll} - \vartheta_{apc}) \tag{31}$$

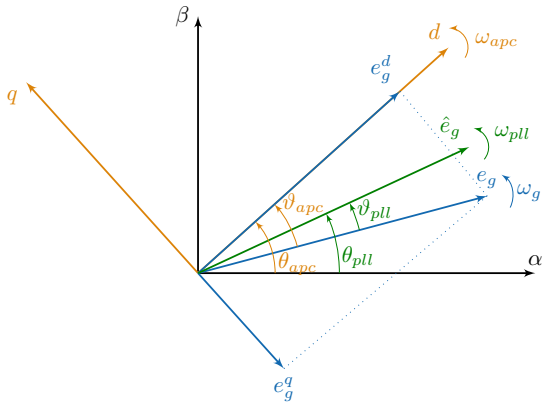

Fig. 3: Vector diagram representing the alignment of different reference frames.

III. Small-Signal Modeling

A full state-space model of the VSC control scheme can be established by reducing the equations (3)-(31), which yields a following 15^{th} order state-space system:

$$\boldsymbol{x} = \left[\boldsymbol{e}_g^{dq},\, \boldsymbol{i}_g^{dq},\, \boldsymbol{i}_s^{dq},\, \boldsymbol{\xi}^{dq},\, \boldsymbol{\gamma}^{dq},\, \varepsilon,\, \vartheta_{apc},\, \vartheta_{pll},\, \tilde{p},\, \tilde{q}\right]^T \tag{32}$$

$$\boldsymbol{u} = \left[p^*,\, q^*,\, v^*,\, v_g,\, \omega_n,\, \omega_g\right]^T \tag{33}$$

where $\boldsymbol{x}$ and $\boldsymbol{u}$ denote the state and input vectors, respectively. For the virtual inertia emulation, the state $\tilde{p}$ is replaced with ν_{apc}, as described in Section II-C. The input vector includes the outer control loop setpoints $(p^*,\, q^*,\, v^*,\, \omega_n)$, as well as the voltage amplitude (v_g) and frequency (ω_g) of the grid equivalent. Hence, the linearized small-signal state-space model can be defined in the general form as:

$$\Delta\dot{\boldsymbol{x}} = \boldsymbol{A}\Delta\boldsymbol{x} + \boldsymbol{B}\Delta\boldsymbol{u} \tag{34}$$

where Δ indicates a small-signal deviation around the linearization point $(\boldsymbol{x}_0,\, \boldsymbol{u}_0)$.

In order to validate the proposed control structure, a nonlinear model was developed in MATLAB Simulink, with the use of a Simscape Power Systems library for the electrical system design. Subsequently, the response to a 10% step change in power setpoint was compared against the full DAE and small-signal models. The results presented in Fig. 4 verify the accuracy of the proposed mathematical formulation, with the small-signal model having better initialization behavior due to aforementioned linearization.

IV. Results

A. Forming vs. Feeding: A Stability Study

The first stability study is conducted through eigenvalue analysis of the proposed small-signal system in (34), with a focus on different converter modes (g-form vs. g-feed) and APC implementation (droop vs. VIE). The APC scheme plays no role in stability of a g-form unit under initial steady-state conditions, since the PLL is not active and the grid frequency is established directly by the VSC. On the other hand, the VIE control scheme in g-feed operation has the slowest response, but provides the highest damping. This can be explained with explicit terms for inertia and damping in (14). The root loci spectrum for all possible configurations is presented in Fig. 5.

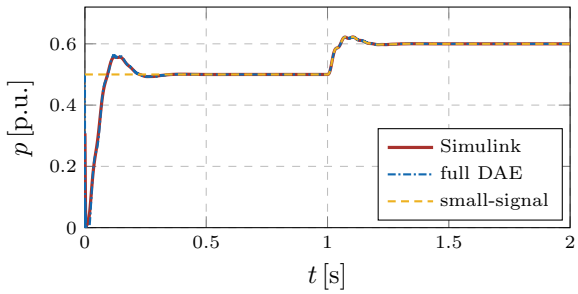

Fig. 4: Transient response of different developed models to a step change in active power setpoint.

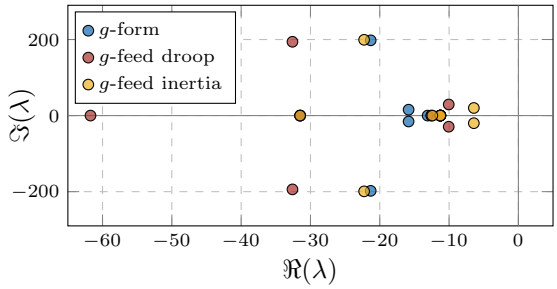

Fig. 5: Root loci spectrum of interest for different converter operation modes.

B. Bifurcation Analysis

We now investigate the impact of APC gains by varying two different sets of parameters: the droop gains (D_p, D_q) of APDC and the virtual inertia and damping constants (H, K_d) in VIE. The stability maps depicted in Fig. 6 indicate that under traditional droop parametrization of $D_p \in [1\%, 5\%]$, all VSC operation modes should preserve stability. However, only the grid-forming converter possesses the capability of meeting potentially higher power response requirements, e.g., $D_p > 10\%$. On the other hand, the VIE-based g-feed unit has higher stability margins for the equivalent damping gains $(K_d < 10\,\text{p.u.})$, i.e., yields lower critical inertia constants $(\hat{H})$.

This property, however, stands only for damping values above 1.85 p.u. Similar findings are showcased in Fig. 7, where the movement of critical eigenvalues $(\hat{\lambda})$ under different virtual inertia levels and unity damping has been observed. As system inertia reduces below 50 ms, the eigenvalues gradually move

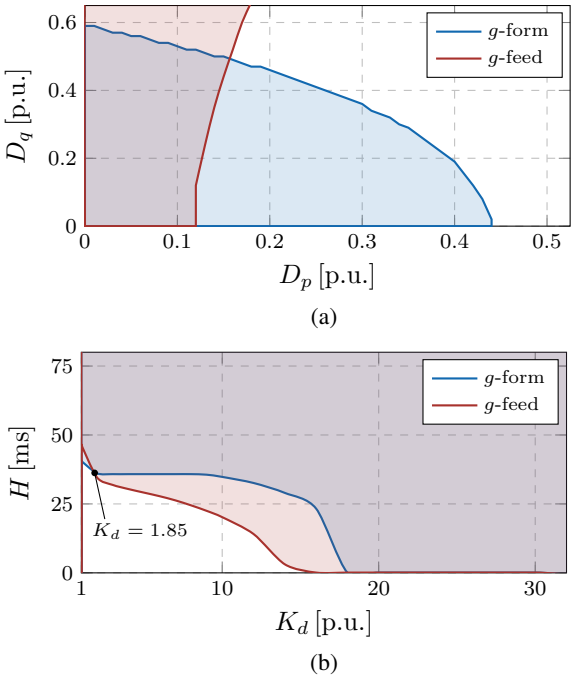

Fig. 6: Stability maps of different converter modes; the system is stable within the shaded region: (a) stability map on the D_p-D_q plane; (b) stability map on the H-K_d plane.

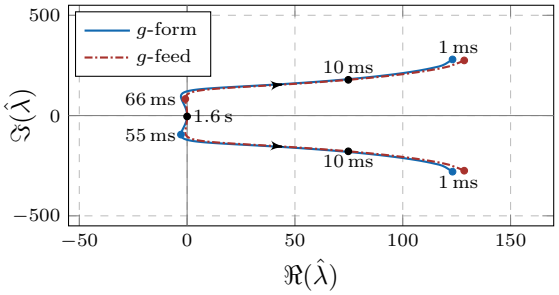

Fig. 7: Movement of the critical eigenvalue $(\hat{\lambda})$ under different inertia levels and converter operation modes.

to the right-hand side of the imaginary plane, resulting in $\hat{H} = 40.6\,\text{ms}$ and $\hat{H} = 46.5\,\text{ms}$ for the g-form and g-feed VSC, respectively.

C. Impact of the Grid Equivalent

In order to study the effect of grid strength on stability of a grid-feeding converter, different Short Circuit Ratios (SCRs), have been considered. The SCR is expressed as $\eta = x_g^{-1} \in [0, 20]$, and incorporated in the model by changing the grid resistance and inductance, while preserving the transmission system ratio $X_g/R_g = 10$. The critical SCRs $(\hat{\eta})$ presented in Fig. 8a confirm that VSCs connected to typical high-voltage systems, usually described with $\eta \approx 3$, are capable of withstanding the traditional droop control gains of up to 5%. However, a faster provision of frequency reserves would be possible only in a very stiff grid, closer to an infinite bus $(\eta > 15)$. On the other hand, having a VIE controller gives operational flexibility, since such g-feed unit can operate even in a very weak network $(\eta < 0.1)$, as shown in Fig. 8b.

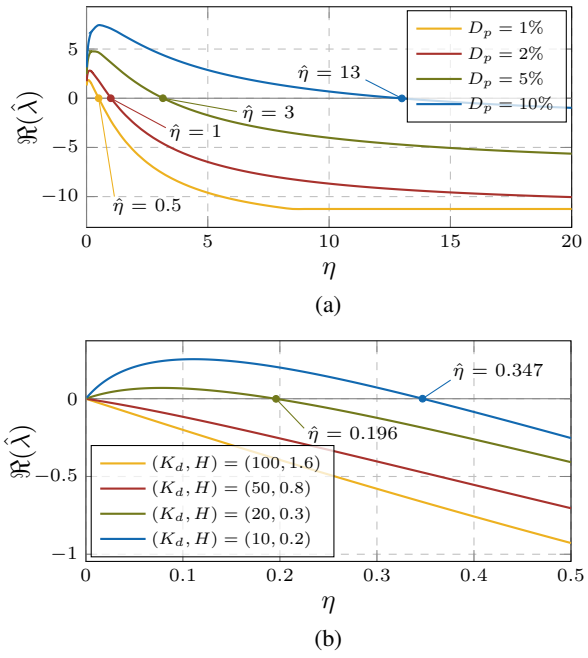

Fig. 8: SCR influence on the stability of a g-feed unit under different active power controllers: (a) APDC; (b) VIE.

V. Conclusion

In this paper, a small-signal stability analysis of converter control modes in low-inertia power systems is investigated. In particular, a detailed VSC control scheme is proposed in a DAE form, and an eigenvalue analysis of the linearized state-space system is performed. Both grid-forming and grid-feeding concepts have been considered, together with different active power controllers based on droop and VIE. It was shown that the stability margins of proposed configurations can vary significantly with respect to parameter sensitivity and robustness. Furthermore, the strength of the grid equivalent can impose constraints on the optimal tuning of converters, especially in case of a droop-based grid-feeding unit. The future work will focus on multi-converter systems and the potential interactions between them, as well as the stability in the presence of conventional synchronous machines.

References

[1] A. Ulbig, T. S. Borsche, and G. Andersson, "Impact of low rotational inertia on power system stability and operation," *IFAC Proceedings Volumes*, vol. 47, no. 3, pp. 7290 – 7297, 2014.

[2] S. D'Arco, J. A. Suul, and O. B. Fosso, "Control system tuning and stability analysis of virtual synchronous machines," in *2013 IEEE Energy Conversion Congress and Exposition*, Sept 2013.

[3] ——, "Small-signal modelling and parametric sensitivity of a virtual synchronous machine," in *2014 Power Systems Computation Conference*, Aug 2014.

[4] ——, "A virtual synchronous machine implementation for distributed control of power converters in smartgrids," *Electric Power Systems Research*, vol. 122, pp. 180–197, 2015.

[5] N. Pogaku, M. Prodanovic, and T. C. Green, "Modeling, analysis and testing of autonomous operation of an inverter-based microgrid," *IEEE Transactions on Power Electronics*, vol. 22, no. 2, pp. 613–625, March 2007.

[6] T. Green and M. Prodanovic, "Control of inverter-based micro-grids," *Electric Power Systems Research*, vol. 77, no. 9, pp. 1204 – 1213, 2007, distributed Generation.

[7] J. Rocabert, A. Luna, F. Blaabjerg, and P. Rodrguez, "Control of power converters in ac microgrids," *IEEE Transactions on Power Electronics*, vol. 27, no. 11, pp. 4734–4749, Nov 2012.

[8] R. Ofir, U. Markovic, P. Aristidou, and G.Hug, "Droop vs. virtual inertia: Comparison from the perspective of converter operation mode," in *2018 IEEE International Energy Conference (ENERGYCON)*, June 2018.

[9] U. Markovic, O. Stanojev, P. Aristidou, and G. Hug, "Partial grid forming concept for 100% inverter-based transmission systems," in *2018 IEEE Power and Energy Society General Meeting (PESGM)*, Aug 2018.

[10] S.-K. Chung, "A phase tracking system for three phase utility interface inverters," *IEEE Transactions on Power Electronics*, vol. 15, no. 3, pp. 431–438, May 2000.

[11] H. P. Beck and R. Hesse, "Virtual synchronous machine," in *2007 9th International Conference on Electrical Power Quality and Utilisation*, Oct 2007.

[12] J. Driesen and K. Visscher, "Virtual synchronous generators," in *2008 IEEE Power and Energy Society General Meeting - Conversion and Delivery of Electrical Energy in the 21st Century*, July 2008.

[13] X. Wang, Y. W. Li, F. Blaabjerg, and P. C. Loh, "Virtual-impedance-based control for voltage-source and current-source converters," *IEEE Transactions on Power Electronics*, vol. 30, no. 12, pp. 7019–7037, Dec 2015.

[14] S. D'Arco, J. A. Suul, and O. B. Fosso, "Virtual synchronous machines - classification of implementations and analysis of equivalence to droop controllers for microgrids," in *2013 IEEE Grenoble Conference*, June 2013.

[15] J. C. Vasquez, J. M. Guerrero, A. Luna, P. Rodriguez, and R. Teodorescu, "Adaptive droop control applied to voltage-source inverters operating in grid-connected and islanded modes," *IEEE Transactions on Industrial Electronics*, vol. 56, no. 10, pp. 4088–4096, Oct 2009.